optica

Discovering high-performance broadband and broad angle antireflection surfaces by machine learning

Sajad Haghanifar,[1] Michael McCourt,[2] Bolong Cheng,[2] Jeffrey Wuenschell,[3] Paul Ohodnicki,[3] and Paul W. Leu[1,4,5,*]

[1]Department of Industrial Engineering, University of Pittsburgh, Pittsburgh, Pennsylvania 15261, USA
[2]SigOpt, San Francisco, California 94104, USA
[3]National Energy Technology Laboratory, U.S. Department of Energy, Pittsburgh, Pennsylvania 15236, USA
[4]Department of Mechanical Engineering and Materials Science, University of Pittsburgh, Pittsburgh, Pennsylvania 15261, USA
[5]Department of Chemical Engineering, University of Pittsburgh, Pittsburgh, Pennsylvania 15261, USA
*Corresponding author: pleu@pitt.edu

Received 10 January 2020; revised 10 May 2020; accepted 13 May 2020 (Doc. ID 387938); published 9 July 2020

Eliminating light reflection from the top glass sheet in optoelectronic applications is often desirable across a broad range of wavelengths and large variety of angles. In this paper, we report on a combined simulation and experimental study of single-layer films, nanowire arrays, and nanocone arrays to meet these antireflection (AR) needs. We demonstrate the application of Bayesian learning to the multiobjective optimization of these structures for broadband and broad angle AR and show the superior performance of Bayesian learning to genetic algorithms for optimization. Our simulations indicate that nanocone structures have the best AR performance of these three structures, and we additionally provide physical insight into the AR performance of different structures. Simulations suggest nanocone arrays are able to achieve a solar integrated normal and 65° incidence angle reflection of 0.15% and 1.25%, respectively. A simple and scalable maskless reactive ion etching process is used to create nanocone structures, and etched samples demonstrate a solar integrated normal and 65° reflection of 0.4% and 4.9%, respectively, at the front interface.

https://doi.org/10.1364/OPTICA.387938

1. INTRODUCTION

Optoelectronic devices such as touch screens, phones, tablets, laptops, and light emitting diodes (LEDs) typically consist of a top glass sheet that protects the device from the environment. Antireflection (AR) is important in this glass for improving the outcoupling efficiency of light in displays or LEDs, augmenting the responsivity of sensors, or increasing the power conversion efficiencies of solar modules. AR is often needed across a range of wavelengths such as the visible range or the solar spectrum and is often desired across a wide range of incidence angles. Broad angle AR may increase viewing angles in displays or LEDs or increase power conversion efficiencies in solar modules.

A single-layer (SL) thin film of AR coating can provide for perfect AR at one particular wavelength and normal incidence. However, these thin films cannot demonstrate high AR across a wide range of wavelengths or incidence angles. An alternative approach is to use sub-wavelength nanostructures [1]. Extensive research efforts have been devoted to construct nanostructured AR materials to reduce light reflection [2–4]. These nanostructures have included nanowires (NWs) [4] and nanocones (NCs) [5]. Many NC-like structures have also been fabricated in the literature by methods such as metal dewetting [2], interference lithography [3], soft imprint lithography [4], nanoparticle dip-coating and precursor-derived one-step assembly [6], as well as ultrasonic-assisted solgel [7]. These studies demonstrate the potential of NW and NC arrays in providing broadband and broad angle AR. However, there has yet to be a comprehensive study on the performance limits of these nanostructures. Furthermore, many fabrication methods are limited in scalability due to the need for multiple processing steps, often comprising some sort of patterning followed by etching.

In this paper, we study the optimal AR characteristics of SL films, NW arrays, and NC arrays for minimizing solar integrated reflection across a broad range of wavelengths for normal incidence and wide angle incidence. A Bayesian learning and optimization method is combined with electrodynamic simulations to rapidly search through the parameter space of various structures and determine optimal and near-optimal structures. Bayesian learning outperforms genetic algorithms in determining higher performing structures under the same simulation budget.

We demonstrate that NC arrays exhibit the best performance for both broadband and broad angle AR of these three structures. NW arrays demonstrate performance comparable only to SL thin films, where NWs function as effective media with indices of refraction about the same as the optimal SL thin film. Optimal

NWs have more of a flat disk shape instead of a high aspect ratio wire shape. NCs grade the index of refraction and have the best performance when the bottom of the NCs fill out the surface to provide for a smooth change in index of refraction with the flat glass. The NCs have a narrow optimal or near-optimal angle of 76° to 87°. Our simulations suggest that NC arrays can demonstrate a minimum solar-integrated reflection of 0.15% at normal incidence and 1.25% at 65° incidence or solar-integrated reflection of 0.78% at 65° and 0.23% at normal incidence. We demonstrate and validate the simulation results by fabricating NC structures with maskless reactive ion etching (MRIE) and compare their performance. NC arrays fabricated by the simple and scalable single-step MRIE process demonstrates a 0.4% for normal incidence and reflection of 4.9% at 65° incidence at the front air–glass interface.

2. SIMULATION

The first part of our study focused on electrodynamic simulations to study solar integrated reflection. We focused on minimizing two objective functions: the solar integrated reflection across the wavelengths 280–1200 nm at (1) normal incidence ($R_{\text{solar},0^\circ}$) and (2) 65° incidence angle ($R_{\text{solar},65^\circ}$). The solar integrated reflection R_{solar} is calculated from

$$R_{\text{solar}} = \frac{\int b_s(\lambda) R(\lambda) \mathrm{d}\lambda}{\int b_s(\lambda) \mathrm{d}\lambda}, \tag{1}$$

where $R(\lambda)$ is the reflection spectrum or the reflection as a function of wavelength λ, and $b_s(\lambda)$ is the photon flux density of the AM1.5 global solar spectrum [8]. $R_{\text{solar},65^\circ}$ is calculated by averaging the solar-integrated reflection for transverse electric (TE)-incident light and transverse magnetic (TM)-incident light at 65°. Assuming normal incidence light at solar noon, an incidence angle of 65° corresponds to 4 h 20 min before and after solar noon.

Figure 1 shows schematics of the three types of structures studied: (a) SL films, (b) NW arrays, and (c) NC arrays. The SL film is defined by only its thickness t. For the SL film, the material was assumed to have a wavelength-independent index of refraction that is the geometric mean of the materials on its sides, $n_1 = \sqrt{n_0 n_2}$. In this work, $n_1 = 1.21$ was used for the SL film, since $n_0 = 1$ for air and $n_2 = 1.46$ for glass. The NW array is defined by its pitch (a), height (h), and diameter (d). The NC arrays are defined by four variables: pitch (a), height (h), top diameter (d_{top}), and bottom diameter (d_{bot}). In the special case of $d_{\text{top}} = d_{\text{bot}}$, the NC array is a NW array. The domains over which the optimization took place for the NW array was $a \in [1, 400]$ nm, $d \in [1, 400]$ nm, and $h \in [1, 800]$ nm with the constraint $d \le a$. For the NC array, the domains were $a \in [1, 400]$ nm, $d_{\text{bot}} \in [1, 400]$ nm, $d_{\text{top}} \in [1, 400]$ nm, and $h \in [1, 800]$ nm with the following constraints: $d_{\text{bot}} \le a$ and $d_{\text{top}} \le d_{\text{bot}}$. The NW and NCs are assumed to be glass.

The finite difference time domain (FDTD) method [9] was used for optical simulations. Simulations were set up so that the reflection from only a single air–glass interface was measured. Please see Supplement 1 for simulation details. Our goal in running these simulations is to search for the solution to

$$\min_{\boldsymbol{x} \in \mathcal{X}} \; R_{\text{solar},0^\circ}(\boldsymbol{x}),\; R_{\text{solar},65^\circ}(\boldsymbol{x}), \tag{2}$$

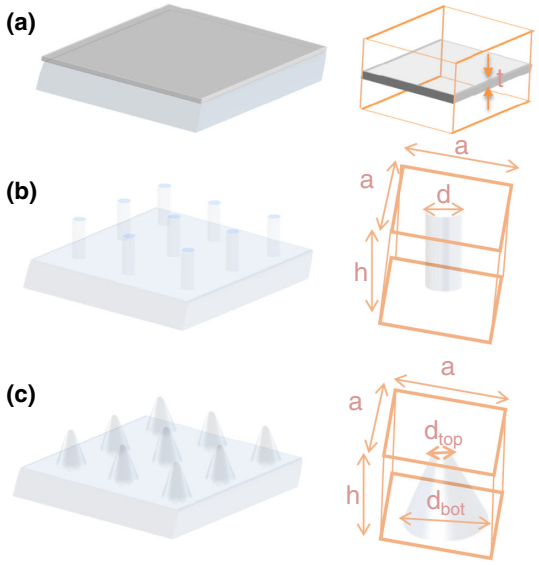

Fig. 1. Schematic of (a) SL thin films, (b) NW arrays, and (c) NC arrays.

where $\mathcal{X}$ is the space of all viable choices of the design parameters (those that satisfy the constraints stated above). In this setting, where there are two competing metrics, we develop a multiobjective Bayesian optimization strategy.

3. MACHINE LEARNING STRATEGY

Unlike a scalar optimization problem, a multiobjective optimization problem does not have a single globally optimal value/solution (except in degenerate cases). In searching for our approximate solution to Eq. (2), we seek to approximate the *Pareto frontier* [10] of objectives $R_{\text{solar}0^\circ}$ and $R_{\text{solar},65^\circ}$. The Pareto frontier is the set of all efficient fabrication configurations, where efficiency is defined as the inability to improve one objective without hurting the other. In finding these configurations, we are able to identify the best possible fabrication strategies and understand how $R_{\text{solar},0^\circ}$ and $R_{\text{solar},65^\circ}$ compete with each other. The actual frontier, in theory, often contains infinitely many points, and as such, we have the ability only to approximately identify points as efficient.

We seek to develop a strategy that effectively approximates the frontier in as few simulations as possible; such a strategy is referred to as *sample efficient* in contrast to so-called *big data* methods. Bayesian optimization (abbreviated BO, but also referred to as Bayesian active optimization) is a sample efficient method for optimizing black-box objective functions [11]. BO methods applied in this situation balance a desire to learn how the structure parameters influence the reflection with a desire to more completely refine the knowledge regarding the minimal reflection values. Standard BO consists of two components: a *probabilistic model*, to model the objective function f, and an *acquisition function*, to determine which parameters $\boldsymbol{x}$ to sample next.

In a standard BO setting, the objective function f is assumed to be a realization of a Gaussian process (GP) with mean function μ and a positive definite covariance kernel K, i.e., $f \sim \mathcal{GP}(\mu, K)$ [12,13]. The mean and covariance functions are defined to have hyperparameters, such as length scales, which are learned through strategies such as maximum likelihood estimation. In all of our modeling, we assume our GPs to have constant mean $\mu(\boldsymbol{x}) = A$

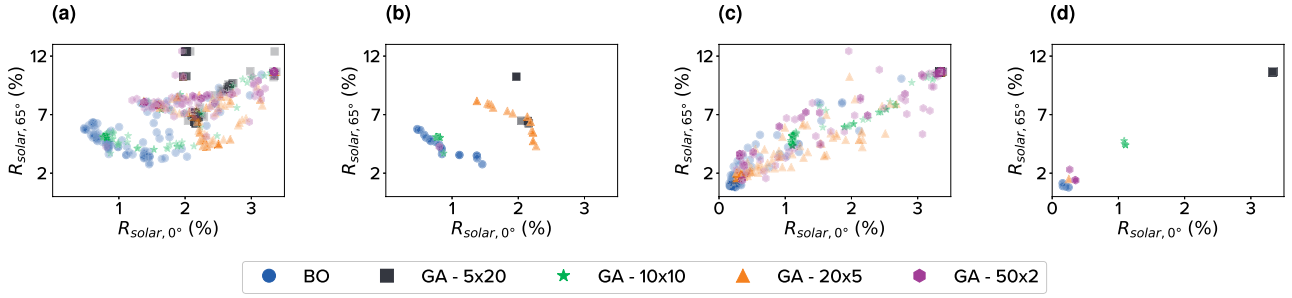

Fig. 2. Strategy described in Section 3 (denoted BO) is compared to the genetic algorithm NSGA-II (denoted GA) with different population sizes (e.g., 5×20 has a population size 5 with 20 generations). Each algorithm was given an evaluation budget of only 100 simulations. For both the nanowire and nanocone simulations, the Pareto frontier of the BO algorithm dominates the Pareto frontiers of all the GA variants: (a) nanowire, all results, (b) nanowire, Pareto frontier, (c) nanocone, all results, and (d) nanocone, Pareto frontier.

(A is fit using generalized least squares) and a C^4 Matérn kernel K with independent length scales in each dimension. A Tikhonov regularization (noise variance) parameter is fixed to be 10^{-3}, mainly to avoid ill-conditioning.

An acquisition function is a utility function that measures the value of sampling at different points within $\mathcal{X}$, given the observed data. Acquisition functions balance the tradeoff between *exploitation*, suggesting parameters near where we have observed the best results so far, and *exploration*, suggesting parameters in regions where we have not sampled. After n different input parameters have been tested, the nth probabilistic model can be created. The maximal argument of the acquisition function determines the next design parameters $\boldsymbol{x}$.

We describe our adaptation of BO to efficiently search for the Pareto optimal set of design parameters. The strategy is derived from the *ϵ-constraint method* [14]. We reformulate the multiobjective optimization problem Eq. (2) as two constrained scalar optimization problems:

$$\min_{x\in\mathcal{X}} \; R_{\text{solar},0^\circ}(x), \;\; \text{s.t. } R_{\text{solar},65^\circ}(x) \geq \hat{R}_{\text{solar},65^\circ}, \tag{3a}$$

$$\min_{x\in\mathcal{X}} \; R_{\text{solar},65^\circ}(x), \;\; \text{s.t. } R_{\text{solar},0^\circ}(x) \geq \hat{R}_{\text{solar},0^\circ}, \tag{3b}$$

where $\hat{R}_{\text{solar},0^\circ}$ and $\hat{R}_{\text{solar},65^\circ}$ are thresholds. By changing $\hat{R}_{\text{solar},0^\circ}$ and $\hat{R}_{\text{solar},65^\circ}$ throughout the optimization, we can discover different sections of the Pareto efficient frontier.

In particular, we adapt techniques from the constrained BO literature [15,16]. After k simulation runs have been observed, two independent GP models $s_{0,k}$ and $s_{65,k}$ are created for reflection at 0° and 65°, respectively. Using these models, an acquisition function is defined for each component of Eq. (3). This acquisition function is modified from the *expected improvement* [17] to account for the desire for viability. Considering, at first, only the solution to Eq. (3a), imposing the viability requires us to consider not only the distribution of $r_0 \sim s_{0,k}(\boldsymbol{x})$ (a Gaussian distribution), but the joint distribution $r_0, r_{65} \sim s_{0,k}(\boldsymbol{x}), s_{65,k}(\boldsymbol{x})$. The acquisition function is defined as

$$a_{R_{\text{solar},0^\circ},k}(\boldsymbol{x}) = \mathbb{E}_{r_0,r_{65}\sim s_{\text{n},k}(\boldsymbol{x}),s_{\text{u},k}(\boldsymbol{x})}\left[(\tilde{r}_{0,k} - r_0)_+ I_{r_{65}\geq\hat{R}_{\text{solar},65^\circ}}\right], \tag{4}$$

where $\tilde{r}_{0,k}$ is the lowest $R_{\text{solar},0^\circ}$ value observed thus far, $(\xi)_+$ denotes $\max(\xi, 0)$, and I_ν is the indicator function. In other words, we are maximizing the expected improvement for viable points; points that do not satisfy the threshold, contribute zero improvement. An analogous acquisition function $a_{R_{\text{solar},65^\circ},k}$ can similarly be defined—the BO algorithm proceeds to choose the next $\boldsymbol{x}$ at which to run a simulation by alternating between maximizing $a_{R_{\text{solar},0^\circ},k}$ and maximizing $a_{R_{\text{solar},65^\circ},k}$.

Since our design parameter space $\mathcal{X}$ has linear constraints, we employ a multistart quasi-Newton optimizer that can take these constraints into consideration when optimizing the acquisition function, namely, sequential least square programming (SLSQP) [18,19]. This ensures that all suggestions made by our algorithm are feasible. We also implement a hit-and-run sampling method for generating points within the constrained space for initializing the optimizer [20]. The BO algorithm is initialized with 10 such randomly chosen points.

4. ANALYSIS OF RESULTS

To empirically demonstrate the performance of this BO algorithm, we compare our method against a popular multiobjective genetic algorithm NSGA-II (as natively implemented in MATLAB through the function gamultiobj) [21,22]. Figure 2 plots the results of this comparison. A total optimization budget of 100 simulations was used; we see that our multiobjective BO method produces a better Pareto frontier than NSGA-II for both the NW and NC simulations. The performance of genetic algorithms is highly sensitive to the population size used: a small population size may be trapped in local minima, while a large population size can find a better optimum but requires more generations to converge. Figure 2 shows the effect of population size for a fixed function evaluation budget of 100. Four different population sizes and number of generations were considered: 5 (population size) $\times 20$ (number of generations), 10×10, 20×5, and 50×2. For both the NW and NC array simulations, the Pareto frontier of the BO algorithm dominates the Pareto frontiers of all the GA variants.

Subsequently, BO was performed with a budget of 500 simulations for the NW and NC arrays. For the SL film, the thickness of the films was changed from 0 nm to 800 nm in 10 nm increments. Figure 3 shows the scatter plot and Pareto frontier of $R_{\text{solar},0^\circ}$ (x axis) and $R_{\text{solar},65^\circ}$ (y axis) for (a) SL films, (b) NW arrays, and (c) NC arrays. The performance of bare glass is shown for reference in each of these plots with a purple box. Figure 3(d) compares the Pareto frontier of the SL films, NW arrays, and NC arrays. The SL films, NW arrays, and NC arrays all show better performance than bare glass. The Pareto points for the SL films and NW arrays show

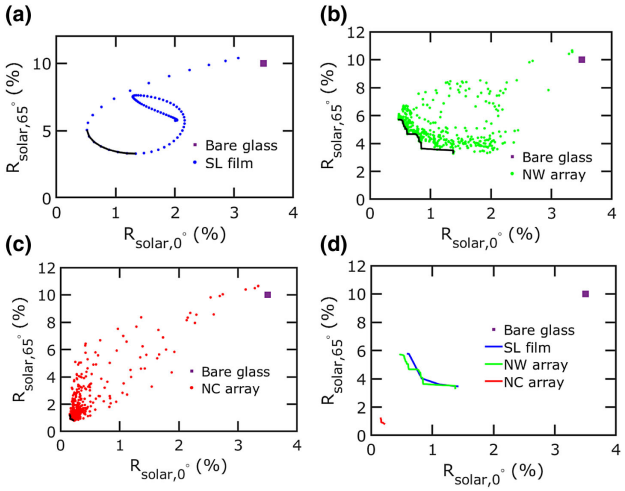

Fig. 3. Scatter plots and Pareto frontier of $R_{\text{solar},0^\circ}$ and $R_{\text{solar},65^\circ}$ for (a) SL films, (b) NW, and (c) NC arrays. (d) Comparison of the Pareto frontier for all structures.

comparable performance, and there is no significant difference between the Pareto line for these two systems. Overall, NC arrays demonstrate the best broadband and broad angle AR properties. NC arrays can demonstrate a minimum $R_{\text{solar},0^\circ} = 0.15\%$ with corresponding $R_{\text{solar},65^\circ} = 1.25\%$ or minimum $R_{\text{solar},65^\circ} = 0.78\%$ with corresponding $R_{\text{solar},0^\circ} = 0.23\%$.

Next, we performed some post-hoc analysis of the computations conducted during the search for the efficient frontier; we analyze the effect of geometry on optimal or near-optimal as defined by Pareto efficiency. Here, near-optimality refers to the points being close to a point on the efficient frontier and accounts for some of the numerical error in the simulations due to finite grid size and simulation time. Figure 4 presents the post-hoc analysis of NW array simulations, where Fig. 4(a) provides a parallel axes plot, Fig. 4(b) depicts the approximate Pareto frontier, and Fig. 4(c) identifies a characteristic of the geometry of all the efficient and nearly efficient results. For the NW arrays, efficient solutions appear only with h in the domain [140, 220], despite the full problem domain being [0, 800]. The combination of low height h plus larger diameter d (in consistent proportion to pitch a) suggests that the structures with lowest reflection tend to have more of a flat disk shape than a high aspect ratio wire shape. These structures occupy approximately 41% of the surface of the glass. This fill factor makes the effective index of refraction of these NW arrays (using the effective medium approximation) about 1.28, which is close to 1.21 of an ideal SL film. The NWs function as effective media and thus, overall, can give only about the same performance as an SL film.

Figure 5 provides analogous plots for the NC array simulations that have a very different spread of Pareto efficient outcomes compared to the NW arrays. Of greatest note, Fig. 5(a) indicates that $d_{\text{bot}} = a$ for all efficient configurations. This implies that the reflection is minimized by maximizing the amount of material at the interface between the bottom of the NCs and the glass. From

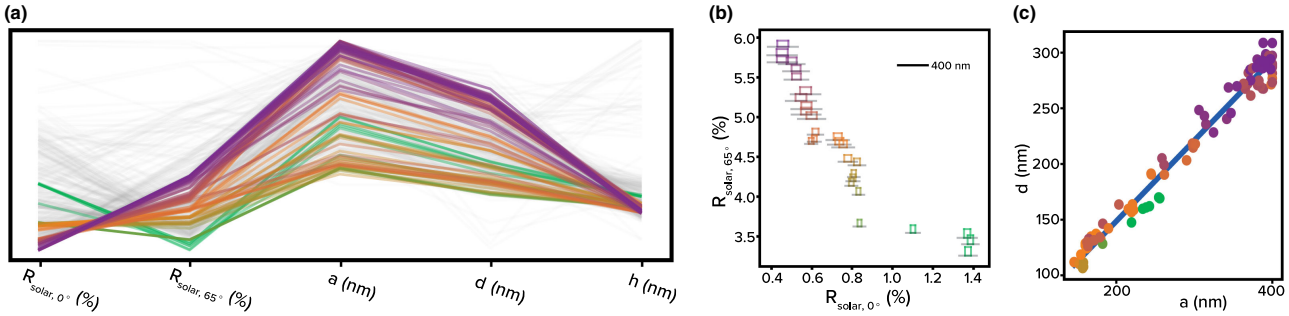

Fig. 4. We applied the strategy described in Section 3 with 500 iterations to approximate the Pareto frontier of Eq. (2) for the nanowire geometry depicted in Fig. 1(b). The parallel axes plot in panel (a) shows the relationship between design parameters a, d, and h and the reflectivity metrics. The colors are defined through the position of the fabrications on the Pareto frontier depicted in panel (b); only a selection of points nearly on the frontier are presented for clarity. In panel (c), a line is fit to the nearly efficient points demonstrating a consistent linear relationship between nanowire diameter and spacing between nanowires.

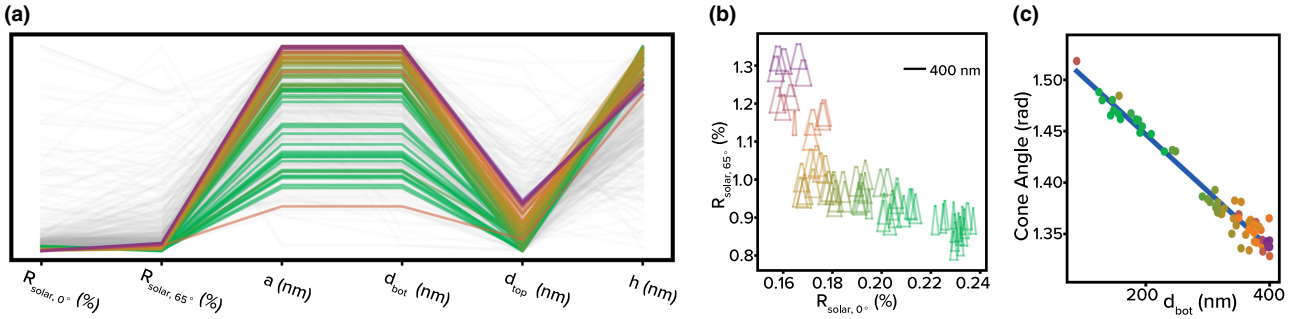

Fig. 5. We applied the strategy described in Section 3 with 500 iterations to approximate the Pareto frontier of Eq. (2) for the nanocone geometry depicted in Fig. 1(c). The parallel axes plot in panel (a) shows the relationship between design parameters a, d_{top}, d_{bot}, and h and the reflectivity metrics. The colors are defined through the position of the fabrications on the Pareto frontier depicted in panel (b). In panel (c), a line is fit to the nearly efficient points demonstrating a consistent linear relationship between nanocone base diameter and the angle of the nanocone.

an effective medium analysis, this minimizes the discontinuity between the bottom of the NC and the top surface of the glass. Figure 5(a) also shows a strong positive correlation (although not a linear relationship) between d_{top}/a and $R_{solar,0°}$. Having a smaller d_{top}/a reduces the discontinuity in the effective index of refraction between the air and the top of the NCs and thus reduces the reflection. Figure 5(b) shows a plot of the nearly efficient outcomes, but with cross sections of the NCs placed along the frontier. In contrast to the NWs, all of the nearly efficient results have a height h in the domain of [600, 790] (note the range was 0 to 800 nm). Figure 5(c) shows the line

$$\text{Cone Angle (rad)} = -0.000552\, d_{bot} + 1.56,$$

fit to the NC's nearly efficient points with $R^2 = 0.965$. These angles all fall within [1.33, 1.52] rad (or 76.2° to 87.1°). The cone angle is computed with

$$\text{Cone Angle (rad)} = \tan^{-1}\left(\frac{2h}{d_{bot} - d_{top}}\right).$$

A different linear relationship is demonstrated in Fig. 4(c) for the NW simulations. The line

$$d = 0.726a + 3.49$$

was fit to the NW's nearly efficient points with $R^2 = 0.980$. This implies that in the NW case, roughly 41% of the surface is covered in NWs.

NC arrays with a morphology similar to near-optimal simulated structures were fabricated on fused silica glass using MRIE methods developed by the authors [23,24] (see Supplement 1). In contrast to other methods in the literature, this is a simple and scalable method that requires only a single process step with no patterning required. The direct etching of nanostructures directly into the glass allows for the structures to be tightly packed together, which simulations suggest enhance AR. Figures 6(a-i) and 6(a-ii) show scanning electron microscopy (SEM) images of a NC array fabricated by MRIE at different magnifications. The AR properties of fabricated samples were characterized by a spectrophotometer. Figure 6(b) compares (i) $R_{0°}(\lambda)$ and (ii) $R_{65°}(\lambda)$ over the wavelength range of 280–1200 nm for bare glass and a fabricated NC array on a single side of the glass. The reflection from the front surface is estimated by assuming incoherence between the front and back surfaces. Please see Supplement 1 for the raw data and calculations. The photon flux density $b_s(\lambda)$ is plotted on the right y axis. The bare glass shows flat behavior in the wavelength range with $R_{solar,0°} = 3.4\%$ and $R_{solar,65°} = 12.5\%$. The fabricated NC array exhibits excellent AR properties with $R_{solar,0°} = 0.4\%$ and $R_{solar,65°} = 4.9\%$. Simulated results are shown for the reflection spectra from bare glass and the NC array. For the NC array, the results are plotted for $d_{top} = 140$, $d_{bot} = 390$, $a = 390$, and $h = 240$ nm. Figure 6(c) shows contour plots of the reflection spectrum as a function of wavelength and incidence angle for (i) the simulated structure and (ii) fabricated NC array. For a wide range of angles and wavelength, and for both simulation and experimental data, the plots are in the blue range, which means that the reflection is less than 5%, and there is a good agreement between simulation and experimental results.

In conclusion, we report using Bayesian learning to find the best AR geometry for different AR coatings of SL films, NW arrays, and NC arrays. We demonstrated that Bayesian learning outperforms genetic algorithms in optimizing these structures for AR. We showed that NC arrays have the best broadband and broad angle AR performance, where the NW arrays and SL films are comparable. Simulated NC arrays can demonstrate a minimum solar-integrated reflection of 0.15% at normal incidence and 1.25% at 65° incidence or solar-integrated reflection of 0.78% at 65° and 0.23% at normal incidence. We also provide physical

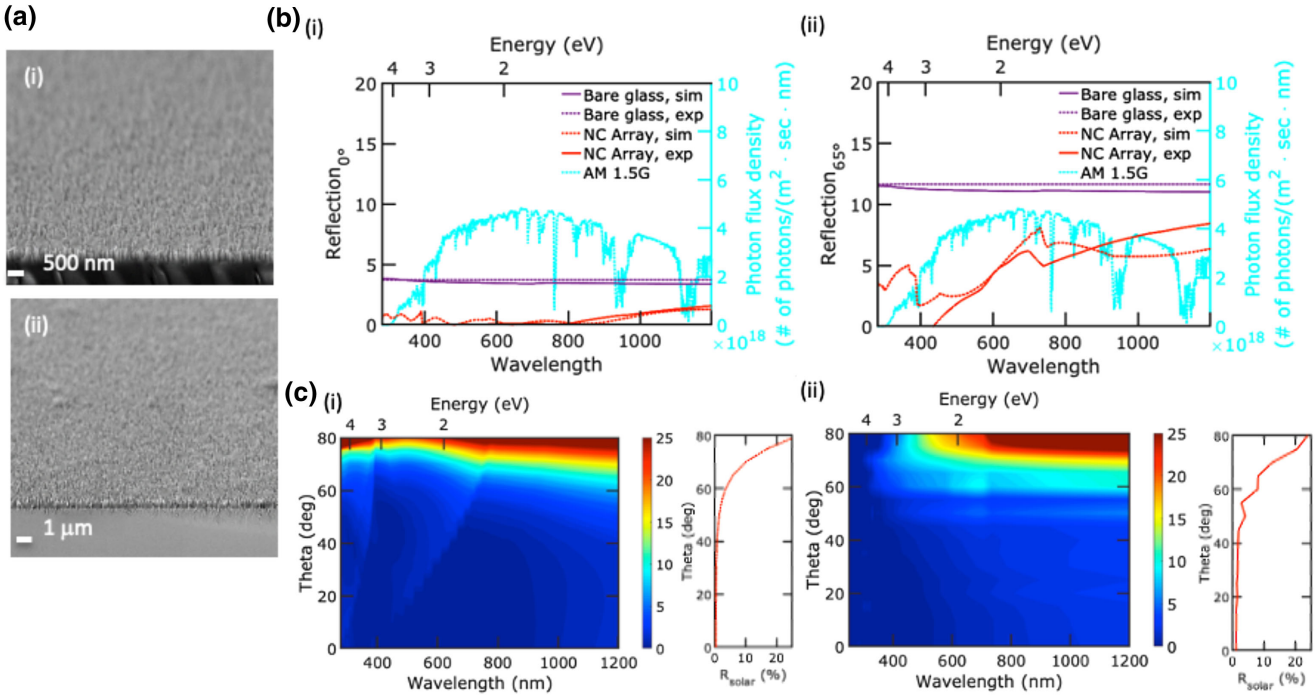

Fig. 6. Experimental NC array results. (a) SEM images of NC array fabricated by MRIE. (b) Experimentally measured and simulated (i) $R_{0°}(\lambda)$ and (ii) $R_{65°}(\lambda)$ for bare glass and NC arrays. (c) R as a function of wavelength and incidence angle for (i) simulations and (ii) experiments.

insight into the performance of the different structures. MRIE fabricated NC arrays on both sides of glass showed a solar integrated reflection of 0.4% for normal incidence and reflection of 4.9% at 65° incidence.

Funding. National Science Foundation (1552712, 1930582).

Acknowledgment. This research was supported in part by the University of Pittsburgh Center for Research Computing through the resources provided. We specifically acknowledge the assistance of Dr. Shervin Sammak.

Disclosures. The authors declare no conflicts of interest.

See Supplement 1 for supporting content.

REFERENCES

1. Z. Han, Z. Jiao, S. Niu, and L. Ren, "Ascendant bioinspired antireflective materials: opportunities and challenges coexist," Prog. Mater. Sci. **103**, 1–68 (2019).
2. D. Infante, K. W. Koch, P. Mazumder, L. Tian, A. Carrilero, D. Tulli, D. Baker, and V. Pruneri, "Durable, superhydrophobic, antireflection, and low haze glass surfaces using scalable metal dewetting nanostructuring," Nano Res. **6**, 429–440 (2013).
3. K.-C. Park, H. J. Choi, C.-H. Chang, R. E. Cohen, G. H. McKinley, and G. Barbastathis, "Nanotextured silica surfaces with robust superhydrophobicity and omnidirectional broadband supertransmissivity," ACS Nano **6**, 3789–3799 (2012).
4. J. van de Groep, P. Spinelli, and A. Polman, "Single-step soft-imprinted large-area nanopatterned antireflection coating," Nano Lett. **15**, 4223–4228 (2015).
5. C. Zhang, W. Li, D. Yu, Y. Wang, M. Yin, H. Wang, Y. Song, X. Zhu, P. Chang, X. Chen, and D. Li, "Wafer-scale highly ordered anodic aluminum oxide by soft nanoimprinting lithography for optoelectronics light management," Adv. Mater. Interfaces **4**, 1601116 (2017).
6. B. Jin and J. He, "Self-templated fabrication of robust moth-eye-like nanostructures with broadband and quasi-omnidirectional antireflection properties," ACS Photon. **4**, 188–196 (2017).
7. I. Zada, W. Zhang, P. Sun, M. Imtiaz, W. Abbas, and D. Zhang, "Multifunctional, angle dependent antireflection, and hydrophilic properties of SiO_2 inspired by nano-scale structures of cicada wings," Appl. Phys. Lett. **111**, 153701 (2017).
8. Solar spectral irradiance: Air mass 1.5.
9. K. Yee, "Numerical solution of initial boundary value problems involving Maxwell's equations in isotropic media," IEEE Trans. Antennas Propag. **14**, 302–307 (1966).
10. M. Ehrgott, *Multicriteria Optimization* (Springer, 2005), Vol. **491**.
11. P. I. Frazier, "Bayesian optimization," in *Recent Advances in Optimization and Modeling of Contemporary Problems*, E. Gel and L. Ntaimo, eds. (INFORMS, 2018), pp. 255–278.
12. C. E. Rasmussen and C. K. I. Williams, *Gaussian Processes for Machine Learning, Adaptive Computation and Machine Learning* (MIT, 2005).
13. G. E. Fasshauer and M. J. McCourt, *Kernel-based Approximation Methods Using MATLAB* (World Scientific, 2015).
14. C. Hwang and A. Masud, "Multiple objective decision making, methods and applications: a state-of-the-art survey," in *Lecture Notes in Economics and Mathematical Systems* (Springer, 1979).
15. M. A. Gelbart, "Constrained Bayesian optimization and applications," Ph.D. thesis (Harvard, 2015).
16. J. Gardner, M. Kusner, Z. Xu, K. Weinberger, and J. Cunningham, "Bayesian optimization with inequality constraints," in *31st International Conference on Machine Learning*, E. P. Xing and T. Jebara, eds., PMLR, Bejing, China, 2014, Vol. **32**, pp. 937–945.
17. D. R. Jones, M. Schonlau, and W. J. Welch, "Efficient global optimization of expensive black-box functions," J. Global Optim. **13**, 455–492 (1998).
18. E. Virtanen and R. Gommers, and SciPy 1.0 Contributors, "SciPy 1.0: fundamental algorithms for scientific computing in Python," Nature Methods **17**, 261–272 (2020).
19. D. Kraft, "A software package for sequential quadratic programming," Technical Report DFVLR-FB 88-28 (DLR German Aerospace Center–Institute for Flight Mechanics, 1988).
20. R. L. Smith, "The hit-and-run sampler: a globally reaching Markov chain sampler for generating arbitrary multivariate distributions," in *28th Conference on Winter Simulation*, IEEE Computer Society, Washington, D.C., USA, 1996, pp. 260–264.
21. *Matlab Global Optimization Toolbox* (The MathWorks, 2019).
22. D. Kalyanmoy, *Multi-Objective Optimization Using Evolutionary Algorithms* (Wiley, 2001).
23. S. Haghanifar, M. McCourt, B. Cheng, J. Wuenschell, P. Ohodnicki, and P. W. Leu, "Creating glasswing butterfly-inspired durable antifogging superomniphobic supertransmissive, superclear nanostructured glass through Bayesian learning and optimization," Mater. Horizons **6**, 1632–1642 (2019).
24. S. Haghanifar, T. Gao, R. T. R. D. Vecchis, B. Pafchek, T. D. B. Jacobs, and P. W. Leu, "Ultrahigh-transparency, ultrahigh-haze nanograss glass with fluid-induced switchable haze," Optica **4**, 1522–1525 (2017).